ORIGINAL ARTICLE

Application of the Failure Assessment Diagram approach for contact fatigue damage evaluation in railway wheel steels

Giorgio Donzella[1] | Andrea Danesi[1] | Angelo Mazzù[1] |
Candida Petrogalli[1] | Andrea Ghidini[2] | Michela Faccoli[1]

[1]Department of Mechanical and Industrial Engineering, University of Brescia, Brescia, Italy

[2]Metallurgy and Laboratories Department, Lucchini RS, Lovere, Italy

Correspondence
Angelo Mazzù, Department of Mechanical and Industrial Engineering, University of Brescia, via Branze 38, 25123 Brescia, Italy.
Email: angelo.mazzu@unibs.it

Abstract

A Failure Assessment Diagram (FAD), developed for rolling contact, was specifically formulated for railway wheel steels. The FAD allows combining a multiaxial fatigue criterion with the linear elastic fracture mechanics concept; in particular, it was used to assess the fatigue failure in wet contact, related to the pressurization of the fluid entrapped in surface cracks. The approach was applied to the results of previous bi-disc tests carried out on three railway wheel steels, subjected first to a dry rolling-sliding contact step, then to a wet contact step. The crack size distribution after the dry contact step was evaluated by a statistical approach; subsequently, the stress intensity factor during the wet contact step was estimated by finite elements. The results of the FAD agreed with the damage observed on the cross section of the specimens at the end of the tests. Furthermore, the FAD was used to determine the maximum allowable crack to prevent rolling contact fatigue, this way showing its potential as a damage tolerant approach.

KEYWORDS
damage tolerance, failure criterion, fracture mechanics, railway wheels, rolling contact fatigue (RCF)

1 | INTRODUCTION

The assessment of damage in the tread of railway wheels is a very complex issue, as many different damage mechanisms can occur, even in competition with each other. They depend on design factors, such as material properties, nominal load, and geometry, as well as on varying working factors, such as train dynamics, load history, and environmental contaminants.

The most common damage phenomenon is wear, intended as a progressive material removal from the wheel tread, approximately uniform along the circumferential direction. Wear is more severe in rolling-sliding condition, which usually occurs in curve or braking. Many models have been used for wear assessment in such conditions, mainly aimed at predicting the tread geometry evolution along with the wear progress (see, for instance, previous studies[1–3]). A well-established

approach for a general assessment of wear in railway wheel is based on the wear maps,[4] which allow determining the grade of wear (classified as "mild," "severe," and "catastrophic") depending on the contact load and wheel-rail sliding speed. Some works highlighted the effect of environmental factors (such as sand[5] or snow and humidity[6,7]), as well as of operational factors (such as shoe braking[3,8,9]) on the wear rate.

Another family of damage mechanism is related to cyclic plasticity, occurring when the elastic shakedown limit is exceeded. Depending on the normal load and the coefficient of friction, cyclic plasticity can occur as a closed-loop plasticization at each load cycle (plastic shakedown) or open-loop plasticization (ratcheting), which leads to unidirectional accumulation of residual plastic strain at each load cycle. In railway wheels, the latter is much more frequent and occurs in conditions of high normal load and sliding, such as, again, in curve or braking. The occurrence of cyclic plasticity can be predicted by means of the well-known shakedown maps; in the case of ratcheting, the accumulation of plastic strain can lead to the formation of surface cracks. Many models were proposed to predict the plastic strain accumulation, mainly based on the critical strain approach[10]: Starting from the calculation of the plastic strain increment at each load cycle, they assume that a crack will be generated once the accumulative plastic strain will reach a critical value, which is a property of the material. Examples of application of such models, taking into account the wheel-rail contact and/or the wheel-brake block contact, can be found in previous studies.[11-13]

Ratcheting alone, usually, is not able to lead to a catastrophic failure. It was shown that, in constant condition of high normal load and sliding, the concomitant effect of ratcheting and wear can lead to a steady-state regime, in which the crack growth is balanced by the removal of the surface layer by wear.[14,15] However, surface cracks generated by ratcheting can become a very serious danger when a driving force enhances their propagation to cause severe shelling. This event can occur even in elastic shakedown regime, which is a condition considered safe by criteria based on the shakedown maps only. The driving force is often related to an external fluid (rain or snow, for instance) that is entrapped inside the cracks and subsequently pressurized when the load passes over the crack mouth. Both the experience[15,16] and laboratory experiments[17,18] showed the detrimental effect of such environmental factor on the fatigue life. The damage in condition of elastic shakedown (e.g., with no cyclic plastic strain) is usually approached in terms of multiaxial fatigue[19,20] or crack propagation.[21,22] The former approach considers fatigue strength an intrinsic material property, neglecting the effect of pre-existing cracks or defects; the latter presumes the pre-existence of a crack, which can propagate or not under the applied load. Indeed, it was shown that in wheel steels pre-existing cracks can affect the fatigue strength only if they exceed a critical size.[23] This suggests that the choice between multiaxial fatigue criteria and crack propagation ones should depend on the sensitivity of the material to the defects.

A unifying approach, which allows considering the combination of the material intrinsic fatigue strength and the effect of pre-existing cracks, is based on the Failure Assessment Diagrams (FAD). The FAD method was first formulated by Dowling and Townley[24] as a static criterion. Subsequently, it was included in several standards, especially for pipes and pressure vessels, and updated several times. Recently, Yu et al.[25] extended this method to the railway field to assess the structural integrity of rails. In their approach, however, they considered a very simplified model, which neglected the origin of the surface cracks, the key role of the fluid, and considered an unrealistic crack geometry.

Recently, Donzella and Petrogalli[26] extended the FAD concept to the structural integrity assessment of components subjected to cyclic contact loading. The basic idea was that under such loading a component can fail either by subcritical propagation of inherent defects, when it is maximally sensitive to their presence, or by high cycle fatigue (HCF), when the effect of the defects is negligible. Between these two failure mechanisms, a transition region can be defined by means of a curve delimiting the fatigue-safe condition from the unsafe one. The latter can be further delimited by curves expressing the transition to cyclic plasticity or critical crack propagation. Subsequently, Donzella et al.[27] extended this method to the assessment of surface hardened components and showed an example of application to roller bearings. In these papers, the material defects were identified as the inherent nonmetallic inclusions: Therefore, they were supposed to be pre-existing, located in the subsurface region, and propagating in Mode II parallel to the contact surface.

In this paper, the FAD concept is specifically formulated for the evaluation of the structural integrity of railway wheels in condition of elastic shakedown. Such condition is usual in straight running, or even in curve when the wheel-rail coefficient of friction is lowered by the presence of water or snow on the contact surface. The fatigue failure mechanism is very different with respect to the case of roller bearings. The nucleation of subsurface cracks, although possible, is a very rare event in railway wheels; therefore, it was neglected in the model. It is proposed that surface cracks have been previously

generated by ratcheting, in events such as braking or curving in dry contact; such cracks are assumed to propagate in mixed mode when subsequent wet contact occurs, driven by the entrapped fluid pressurization mechanism. The FAD can allow evaluating their effect on the fatigue strength of the steel, provided that a specific model is elaborated for assessing the initial crack geometry and the mixed-mode propagation with entrapped fluid. In order to test the effectiveness of the approach, it was used to assess the results of small-scale experiments aimed at simulating the damage occurring in real wheels. A statistical methodology was proposed for determining the typical crack geometry generated by ratcheting in dry contact; furthermore, a calculation procedure was proposed for assessing mixed mode crack propagation with entrapped fluid pressurization.

2 | THE FAD APPROACH FOR ROLLING CONTACT LOADING

2.1 | Theoretic model formulation

The FAD approach for the study of the rolling contact fatigue (RCF) is explained in detail in Donzella and Petrogalli.[26] It is based on the well-known diagram of Kitagawa and Takahashi,[28] which shows that the fatigue strength is scarcely affected by the presence of defects if their size a is small ("short crack" field), whereas it can be well described by a linear elastic fracture mechanics (LEFM) approach if their size is large ("long crack" field). This effect is related to influence of the microstructure on crack propagation when the crack size is comparable to the grain size. The crack size corresponding to the transition from the short to the long crack field depends, therefore, on the material properties.

The LEFM formulation for the propagation threshold is represented by the following expression:

$$\Delta K_{th} = \Delta \sigma_{cr} \sqrt{\pi a}, \tag{1}$$

where ΔK_{th} is the threshold stress intensity factor (SIF) range and $\Delta \sigma_{cr}$ the corresponding applied stress range: $\Delta \sigma_{cr}$ represents the fatigue limit for a component with a crack of size a. For long cracks, ΔK_{th} is a material property only; therefore, the fatigue limit $\Delta \sigma_{cr}$ decreases with trend $(a)^{-0.5}$.

For short cracks, as $\Delta \sigma_{cr}$ scarcely depends on the crack size, the formulation of Equation (1) can be kept if ΔK_{th} is supposed to vary with a in such a way that $\Delta \sigma_{cr}$ is almost constant.

To describe analytically this dependence, El Haddad et al.[29] proposed the following relationship:

$$\Delta K_{th} = \Delta K_{thl.c.} \sqrt{\frac{a}{a + a_0}}, \tag{2}$$

where $\Delta K_{thl.c.}$ is the propagation threshold for long cracks (being, therefore, a material property only), whereas a_0 is an "intrinsic" crack length, which can be obtained by imposing the LEFM formulation of Equation (1) in its classical formulation for long cracks (e.g. with $\Delta K_{th} = \Delta K_{thl.c.}$) to a defect-free component in the threshold condition:

$$a_0 = \frac{1}{\pi} \left(\frac{\Delta K_{thl.c.}}{\Delta \sigma_0} \right)^2, \tag{3}$$

where $\Delta \sigma_0$ is the fatigue limit for a defect-free component ("plain" fatigue limit). Equation (2) expresses the transition from the short crack field to the long crack one: In fact, for $a \to \infty$, $\Delta K_{th} \to \Delta K_{thl.c.}$, whereas, combining Equations (1)–(3), for $a \to 0$, $\Delta \sigma_{cr} \to \Delta \sigma_0$.

Let us now consider a component subjected to rolling contact loading, containing a surface crack with size a (see Figure 1): The SIF range during a contact cycle can be generally written as a function of the applied Hertzian pressure p in the form:

$$\Delta K = y p \sqrt{\pi a}, \tag{4}$$

where y is a correction factor taking into account the contact stresses distribution (both normal and tangential), the possible effect of a lubricant, the crack geometry, and the coefficient of friction f_c between the crack faces.

Considering the correction factor, the intrinsic crack length a_0 in Equation (2) can be replaced by a critical crack length a_D,[30,31] which for rolling contact loading, from Equations (4) and (3), can be expressed in the form:
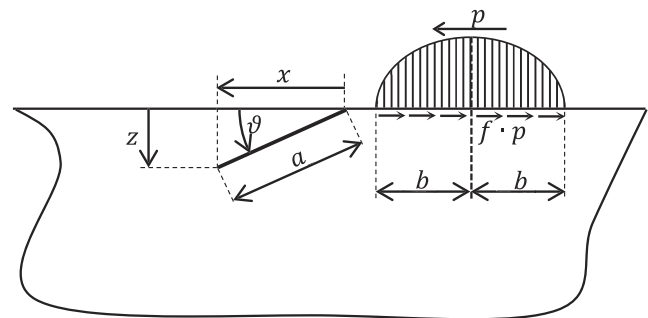

FIGURE 1 Schematic of a cracked body with a traveling Hertz pressure distribution

$$a_D = \frac{1}{\pi} \left(\frac{\Delta K_{thl.c.}}{y \cdot p_0} \right)^2, \tag{5}$$

where p_0 is the Hertz pressure correspondent to the RCF limit for a defect-free component.

The threshold condition $\Delta K = \Delta K_{th}$, with ΔK written in the form of Equation (4), gives the pressure p_{cr} correspondent to the RCF limit for a component with a crack of length a:

$$p_{cr} = \frac{\Delta K_{th}}{y \sqrt{\pi a}} \tag{6}$$

By defining

$$P_p = \frac{p_{cr}}{p_0} \tag{7}$$

$$K_p = \frac{\Delta K_{th}}{\Delta K_{thl.c.}} \tag{8}$$

and combining Equations (8), (7), (6), and (5) with Equation (2) (with a_0 replaced by a_D) the following expression is finally obtained:

$$K_p = \sqrt{1 - P_p{}^2} \tag{9}$$

Equation (9) has the form of a FAD, which defines the RCF failure limit taking into account the different role that defects can have, and is represented by the diagram shown in 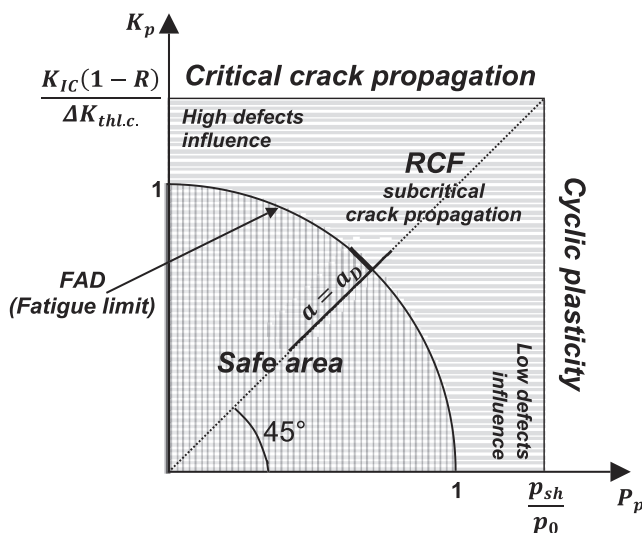Figure 2. This approach constitutes an alternative way of representing the nonlinearity due to the short cracks effect, as well as the correspondent dependence of crack growth threshold on crack size described by the Kitagawa–Takahashi diagram, applied to the RCF.

The point given by $K_p = 1$ and $P_p = 0$ is the fatigue limit calculated according to the LEFM approach, therefore assuming the maximum influence of the defects. The point given by $K_p = 0$ and $P_p = 1$ is the fatigue limit calculated according to the plain fatigue approach, therefore assuming no influence of the defects. The other points lying on the limit curve express the variation of the defect influence, depending on the material properties and defect size. The critical crack size a_D ideally separates the diagram in two zones: the upper one (for $a > a_D$), where the fatigue limit strongly depends on the crack presence, and the lower one (for $a < a_D$) where the fatigue limit weakly depends on the crack presence.

The application of the FAD is formally limited by the applicability field of the LEFM approach, although it was corrected to account for the nonlinearity related to the short crack effect: For this reason, the FAD does not apply in the presence of a macroscopic plasticization. If the elastic shakedown limit is exceeded, this basic requirement is violated; therefore, the condition $P_p \leq p_{sh}/p_0$ has to be fulfilled, where p_{sh} is the elastic shakedown limit pressure for a given coefficient of friction. For railway wheels, when the shakedown limit is exceeded, the damage can be assessed according to the shakedown maps and the models of cyclic plasticity discussed above.

Another limitation of the FAD application is given by the switch from subcritical to critical crack propagation: if the maximum applied SIF during a load cycle (given by $\Delta K/(1 - R)$, R being the load ratio) exceeds the material fracture toughness K_{IC}, the component is expected to fail by monotonic fracture and the fatigue concept does not apply: this leads to the condition $K_p \leq K_{IC}(1 - R)/\Delta K_{thl.c.}$. In railway wheels, exceeding the material fracture toughness implies a structural failure of the whole wheel, which is outside the field of the studied RCF phenomena occurring at the tread.

Therefore, by plotting in the diagram the point representative of the case under examination (called "reference point" in the following) in terms of

$$p_p = \frac{p}{p_0} \tag{10}$$

$$k_p = \frac{\Delta K}{\Delta K_{thl.c.}}, \tag{11}$$

FIGURE 2 Failure Assessment Diagram (FAD): safe and damage areas. RCF, rolling contact fatigue

where p and ΔK are, respectively, the applied contact pressure and SIF range, it is possible to determine if it

falls in the safe zone or, if not, which type of failure the component will experience.

2.2 | Model implementation for railway wheels

The following comments are useful to carry out this assessment on a railway wheel. The limit pressure p_0 is the Hertz pressure corresponding to the occurrence of RCF for a defect-free wheel in the near-surface zone, where RCF damage typically occurs. It can be determined by searching for a relationship of p_0 with the uniaxial material plain fatigue limit $\Delta\sigma_0$, through a stress-based failure criterion.

The orthogonal shear stress criterion[32] is often used for RCF, as the orthogonal shear stress is the only alternated stress component. It gives the same results as the more general Dang Van and Maitournam criterion[33] (which considers the cyclic variation of the whole stress tensor) when the hydrostatic stress influence is negligible, as it was shown to happen in RCF.[34,35]

The p_0 value depends also on the coefficient of friction f on the contact surface, because it changes the stress distribution inside the component. For $f \neq 0$, the orthogonal shear stress has two relative maxima: one on the contact surface and the other one in the subsurface region, approximately at a depth $z \approx 0.5b$. Therefore,

- if the maximum on the contact surface is considered, the p_0 value can be estimated as[35]

$$p_0 = \frac{\Delta\tau_0}{f} \cong \frac{0.29}{f}\Delta\sigma_0 \qquad (12)$$

where the ratio 0.29 between the material shear fatigue limit $\Delta\tau_0$ and the uniaxial fatigue limit $\Delta\sigma_0$ is taken from the fitting of several experimental results for steels obtained by Atzori et al.[36]:

- if the maximum in the subsurface region is considered, the limit fatigue condition can be defined by the von Mises equivalent stress variation, whose relationship with the friction can be obtained by fitting the numerical results obtained by Ren and Glodez,[37] giving

$$p_0 = \left(47.7 \cdot f^3 - 24.6 \cdot f^2 + f + 1.7\right) \cdot \Delta\sigma_0. \qquad (13)$$

In both cases, the uniaxial material fatigue limit $\Delta\sigma_0$ can be approximated by the formula[36]:

$$\Delta\sigma_0 = 2 \cdot 0.475 \cdot \sigma_{uts}, \qquad (14)$$

where σ_{uts} is the material ultimate stress.

The elastic shakedown limit pressure depends on f as well, through the following relationships proposed by Johnson[38]:

- if the stress relative maximum on the contact surface is considered,

$$p_{sh} = 0.58 \cdot \sigma_y/f \qquad (15)$$

- if the stress relative maximum in the subsurface region is considered,

$$p_{sh} = 2.32 \cdot \sigma_y \qquad (16)$$

where σ_y is the material yield stress.

Figure 3 shows the fatigue and elastic shakedown limits in terms of normalized Hertz pressure with varying coefficient of friction, from Equations (13)–(16). Usually, for every f, the lower curve is considered as the limit. Therefore, for the fatigue limit, Equation (13) holds for $f \leq 0.23$ and Equation (12) for $f > 0.23$. For the elastic shakedown limit, Equation (16) holds for $f \leq 0.25$ and Equation (15) for $f > 0.25$. In the FAD approach, however, as the effect of a pre-existing crack is considered, the limits have to be properly chosen based on the crack depth.

In a RCF phenomenon, different propagation modes are usually involved, especially Mode I and Mode II. Among the various models for defining an equivalent SIF range, the following[26] is particularly simple and appropriate for this study:
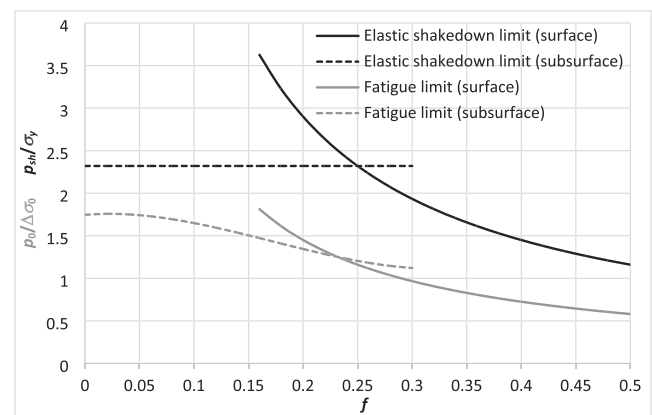
FIGURE 3 Fatigue and elastic shakedown limits in cylindrical contact with varying coefficient of friction

$$\Delta K_{eq} = \sqrt{(1.43 \cdot \Delta K_{I0})^2 + (\Delta K_{II})^2}, \qquad (17)$$

where ΔK_{I0} and ΔK_{II} are the applied SIFs, respectively, in Mode I (only the positive part, correspondent to crack opening) and in Mode II (whole range).

3 | APPLICATION TO EXPERIMENTAL TESTS

In order to show the predictive capacity of the method, the FAD was used to analyze the results of experimental rolling and sliding contact tests recently carried out by Mazzù et al.[17] on discs extracted from railway wheels.

3.1 | Summary of the experimental procedure and results

The tests were carried out by means of a bi-disc machine on three different railway wheel steels used in Europe or in North America for shoe braked wheels: The steels were ER7 EN13262 (designated as HyperLOS® in Mazzù et al.[17]) and AAR Class B and AAR Class B+ (designated as SandLOS® in Mazzù et al.[17]). The chemical composition, the microstructural data, and the mechanical properties of the steels used in the FAD analysis were taken from previous papers of Faccoli et al.[39,40] and are reported in Table 1. Note that the apparent fracture toughness K_Q is given as an approximation of the Mode I fracture toughness K_{IC}, because the size of the wheels from which the specimens were extracted did not allow to comply with the standard requirements for excluding

the influence of the specimen geometry. However, in the following studied cases, this parameter has no influence on the FAD evaluation.

The test procedure was designed to reproduce experimentally the wheel tread damage caused by block braking and subsequent dry and wet contact with the rail. The wheel discs had 80-mm diameter and 20-mm thickness; the rail and brake block discs had 60-mm diameter and 15-mm thickness. They were mounted onto two parallel independent shafts, whose one could displace orthogonally to the rotation axis. The specimens were pushed in contact by means of a hydraulic cylinder, acting on the displaceable shaft. A schematic of the experimental device is given in Figure 4.

Initially, the wheel discs were subjected to 2000 cycles in sliding contact against discs in cast iron used for brake blocks, such as to reach the typical temperature of the wheel tread surface during a stop braking. Subsequently, the wheel discs were subjected to 10,000 cycles in rolling and sliding dry contact against rail discs, with the wheel disc as follower. At the end of these steps, some of the
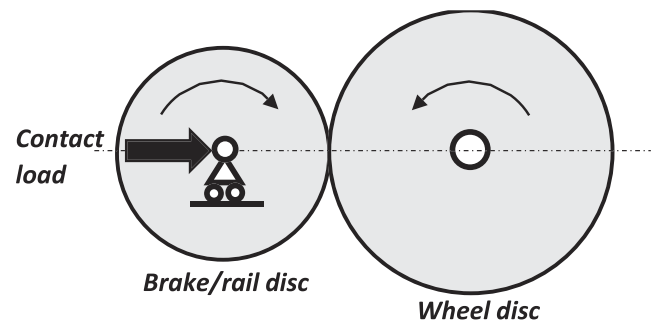

FIGURE 4 Schematic of the specimens on the bi-disc machine

TABLE 1 Chemical composition, microstructural data and mechanical properties of the tested wheel steels, from Faccoli et al.[39,40]

		ER7	Class B	Class B+
Chemical composition (wt%)	C	0.51	0.65	0.63
	Mn	0.78	0.63	0.84
	Si	0.38	0.26	0.88
	S	0.002	0.001	0.001
	P	0.015	0.012	0.009
Microstructure		Pearlite + Ferrite + Bainite (traces)	Pearlite + Ferrite	Pearlite + Ferrite + Bainite (traces)
Grain size number G		8.5	7.5	8.5
Yield strength σ_y (MPa)		568	659	687
Ultimate tensile strength σ_{uts} (MPa)		885	1035	1148
Apparent fracture toughness K_Q (MPa m$^{0.5}$)		102	58	49
Fatigue crack growth threshold $\Delta K_{thl.\,c.}$ (MPa m$^{0.5}$)		8.1	7.1	7.5

wheel discs were cut along the mid plane orthogonally to the contact surface. The cross section was prepared with standard metallographic techniques: It was ground with SiC papers, polished with 1-μm diamond paste and chemically etched by 2% Nital for making the microstructure visible. The microstructural observations were carried out with a light optical microscope to investigate the damage occurred under the contact surface and report the number, length, and inclination of the detected cracks. The grain size number was estimated using the comparison method, according to ASTM E 112 Standard. The remaining intact wheel discs were subsequently subjected to rolling and sliding contact with rail specimens under a jet of water, again with the wheel disc as follower. The duration of the wet step varied from 5000 to 30,000 cycles, in order to investigate the evolution of the wheel disc damage. Again, at the end of the wet step, the wheel discs were cut and subjected to the same metallographic analyses, documenting the damage mechanisms. Moreover, the friction coefficient was measured during the tests. The test parameters relevant for the FAD evaluation, referred to the steps of dry and wet contact between wheel and rail specimens, are summarized

TABLE 2 Working conditions in the different steps of the tests

	Dry step	Wet step
Sliding ratio	1%	
Hertz contact pressure p (MPa)	1100	
Contact half width b (mm)	0.333	
Mean coefficient of friction f	0.4	0.2

in Table 2 (where the sliding ratio is the ratio of the tangential speed to the mean rolling speed). The data referring to the initial contact between the wheel specimens and the brake-block ones are not reported, as they are not relevant for the FAD evaluation; however, further details on the experiments are given in Mazzù et al.[17]

For all the tested steels, the subsurface microstructure after the dry contact step, as shown in Figure 5, was characterized by intense unidirectional plastic flow (ratcheting), induced by the high tangential stresses at the contact surface. Many cracks aligned with the plastic flow bands were observed, counted, and classified based on their size and inclination: While the full results are given in Mazzù et al.,[17] the relevant ones for the FAD assessment were selected and elaborated according to the procedure illustrated in the following.

The specimens that after the dry contact step were subjected to the wet contact step failed by severe RCF. As shown in Figure 6 for the ER7 steel, the surface cracks, nucleated in the previous dry step, propagated progressively with the cycle number, favored by the pressurization of the water entrapped inside the cracks, until they branched and re-emerged causing the detachment of large fatigue debris (shelling). Similar results were obtained with the other tested steels.

3.2 | Evaluation by the FAD approach

The FAD approach was applied to the experimental tests to interpret the results in terms of damage. In the dry step of the tests, the FAD was not applicable because the
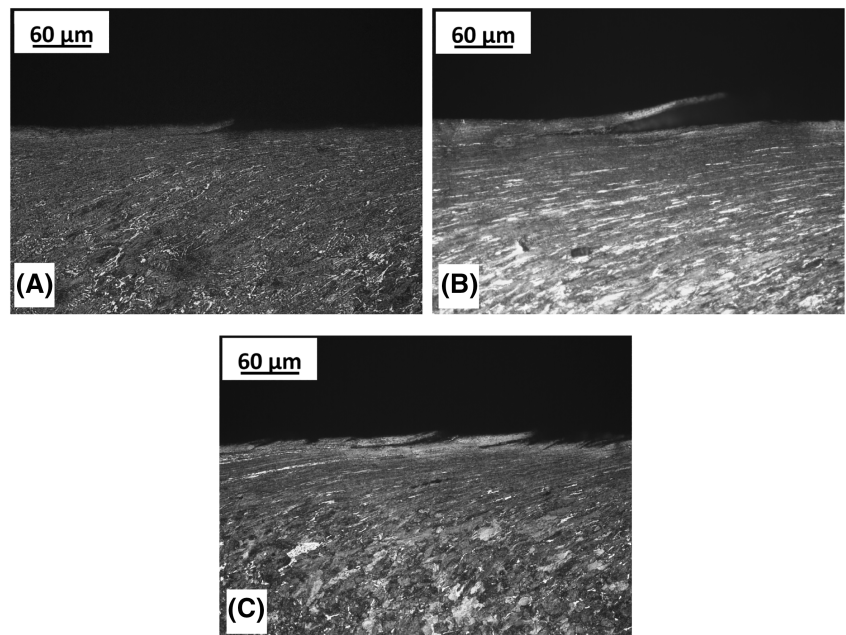

FIGURE 5 Micrographs of the disc cross-section at the end of the dry step of the tests: (A) ER7, (B) Class B, and (C) Class B+
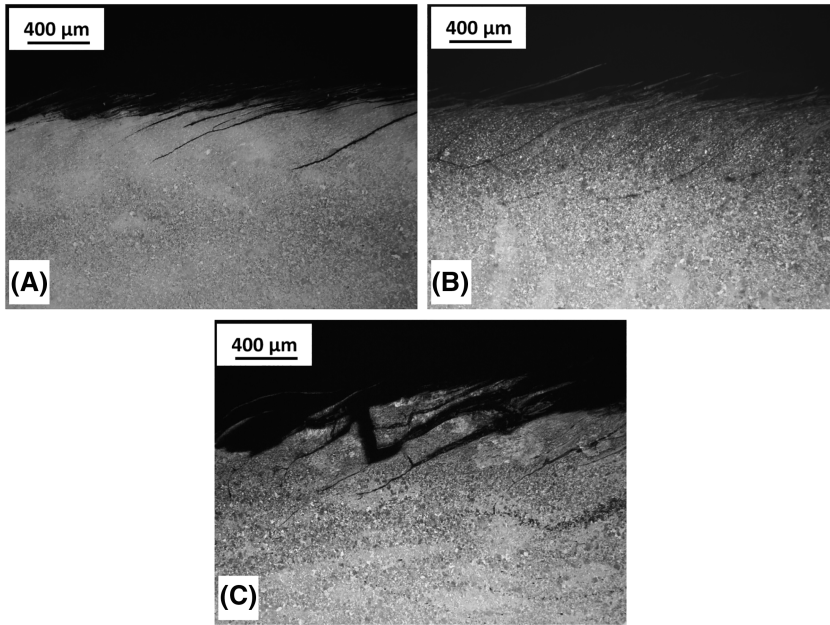
FIGURE 6 Micrographs of the cross sections of the ER7 discs at the end of the wet step of the tests after: (A) 5000 wet cycles, (B) 10,000 wet cycles, and (C) 30,000 wet cycles

working conditions exceeded the elastic shakedown limit. In fact, considering the applied coefficient of friction $f = 0.4$, from Equation (15) the elastic shakedown limit pressures p_{sh} for the three materials were

- ER7: $p_{sh} = 824$ MPa,
- Class B: $p_{sh} = 956$ MPa, and
- Class B+: $p_{sh} = 996$ MPa

all lower than the applied pressure.

In this case, the well-known shakedown map for cylindrical contact[38] can be used to predict the damage: Consistent with the obtained results, the predicted damage was ratcheting.

In the wet step subsequent to the dry step, the coefficient of friction was $f = 0.2$; in this condition, from Equation (15), the elastic shakedown limit pressures have the following values:

- ER7: $p_{sh} = 1647$ MPa,
- Class B: $p_{sh} = 1911$ MPa, and
- Class B+: $p_{sh} = 1992$ MPa

all exceeding the applied pressure: Therefore, at least for the p_p range, the FAD was found to be applicable. Note that Equation (15) was used instead of Equation (16) for determining p_{sh}, despite the latter giving a lower value for $f = 0.2$: indeed, as shown below, the cracks considered for the FAD application have a very shallow depth, therefore the more appropriate limit is the one obtained considering the surface stress maximum.

In order to evaluate the applied k_p, a geometry for the pre-existing crack had to be defined. The cracks

nucleated during the previous dry step were considered as pre-existing at the beginning of the wet step: Obviously, their geometry was not known, but an estimation was done based on the analysis carried out on the specimens cut after the dry step. In Mazzù et al.,[17] a large number of cracks generated by ratcheting in the dry step was measured for each steel; however, most of them were very small and shallow, while the most dangerous for fatigue are the longest ones.

Therefore, a selection of the cracks to be considered for the FAD evaluation was made: Only cracks whose depth z exceeded 20 μm were accounted for. For each steel, the standard distribution of the crack depth $p_z(z)$ was calculated; furthermore, the probability p_n associated with the number of cracks was calculated as follows:

$$p_n = \frac{n_i}{N}, \tag{18}$$

where n_i is the number of cracks detected in each steel and N is the total number of cracks found in all steels. For each material, the combined probability density $p_{zn}(z)$ was calculated as follows:

$$p_{zn}(z) = p_z(z) \cdot p_n \tag{19}$$

as well as the corresponding cumulated probability:

$$P_{zn}(z) = \int_0^z p_{zn}(z) \cdot dz. \tag{20}$$

For each material, $P_{zn}(z)$ gives the probability of finding a crack deeper than z. In order to choose a crack depth

statistically representative of the deepest cracks that can be found in each steel, the depth z for which $P_{zn}(z) = 5\%$ was chosen as the typical crack depth of each material. Figure 7 shows the probability density $p_{zn}(z)$ and cumulated probability $P_{zn}(z)$ of the three steels, as well as the corresponding typical crack depth, which is 27 μm for the ER7, 36 μm for the Class B, and 30 μm for the Class B+.

As far as the crack inclination ϑ is concerned, for each steel the average inclination of the detected experimental cracks was considered: it resulted in $\vartheta = 6.7°$ for the ER7, $\vartheta = 9.1°$ for the Class B, and $\vartheta = 9.4°$ for the Class B+. Figure 8 shows the x and z dimensions of the detected cracks, as well as the typical crack of each steel.

For each critical crack, a finite element (FE) model as the one shown in Figure 9 was built with ABAQUS for calculating the applied SIF during a load pass.

The two contacting discs were approximated by 2-D plane strain bodies, the lower one having a flat contact surface with an inclined crack and the upper one with a cylindrical contact surface. Unilateral contact with penalty method was set between the bodies and the crack faces. The radius of the upper body was

$$R_{eq} = \frac{R_1 \cdot R_2}{R_1 + R_2} = 17.14 \text{ mm}, \quad (21)$$

that is the equivalent radius according to the Hertz model, where $R_1 = 40$ mm and $R_2 = 30$ mm are the radii of the specimens. As the lower body is concerned, the vertical displacements of the lower side and the horizontal displacements of the lateral sides were bounded. As the upper body is concerned, its center was connected with the upper side by rigid beams, and the boundary conditions were imposed on the center. First, a unit contact load of 575.7 N/mm was imposed on the upper body, so as to obtain the same Hertz pressure and contact width as in Table 2; in this phase, only vertical displacements were allowed. Then, while keeping the applied load, a displacement $s = 2$ mm and a rotation $\alpha = s/R_{eq} \cdot 1.01$ were imposed on the center of the upper body, this way imposing the same sliding ratio as in the experimental tests. A friction coefficient $f = 0.2$ was imposed between the two contacting bodies; the same value was assigned to the coefficient of friction between the crack faces: $f_c = 0.2$. The crack tip was modeled with the quarter node technique; the element size was very small near the crack

FIGURE 7 Probability associated with the number and depth of cracks in the tested steels: (A) probability density $p_{zn}(z)$ and (B) cumulated probability $P_{zn}(z)$ [Colour figure can be viewed at wileyonlinelibrary.com]
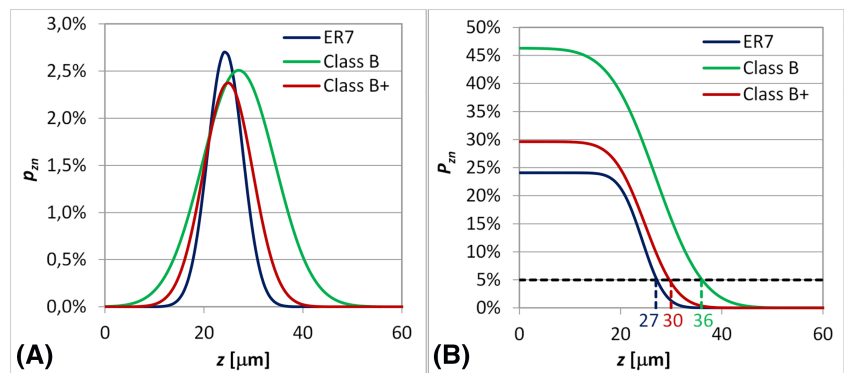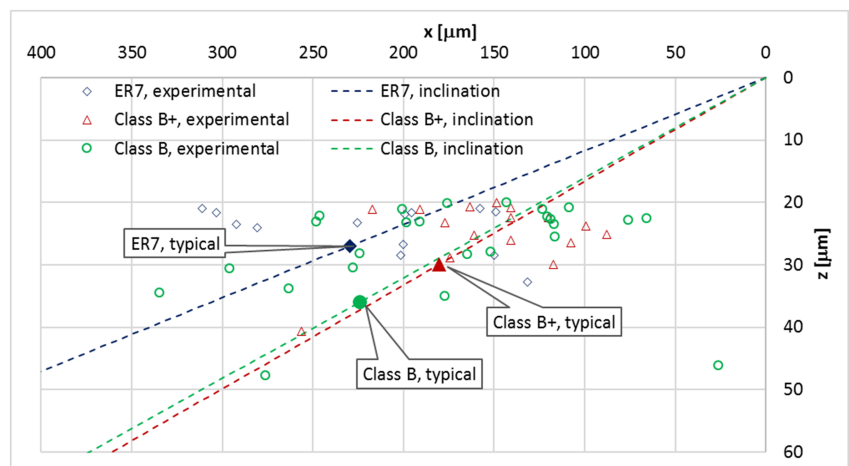

FIGURE 8 x and z dimensions of the experimental and typical cracks and average crack inclinations in the three tested steels [Colour figure can be viewed at wileyonlinelibrary.com]
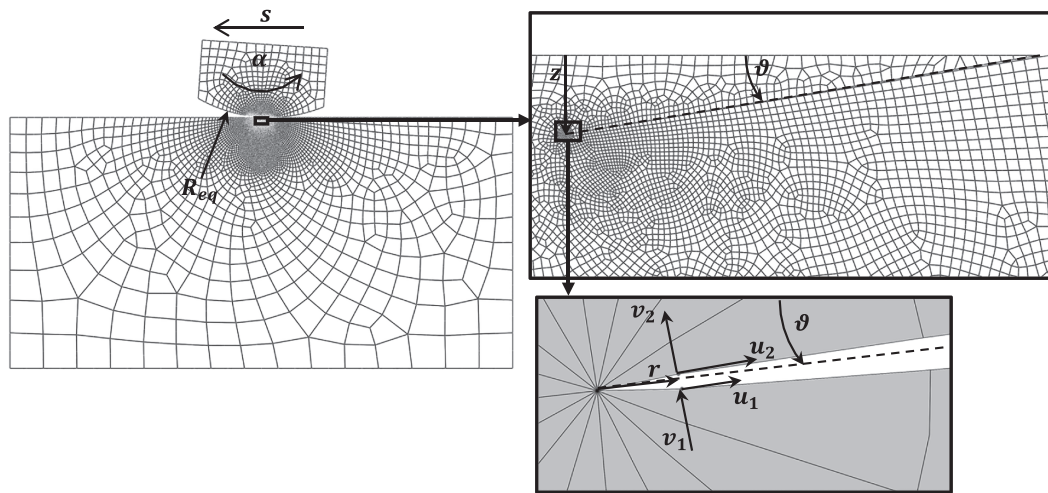
FIGURE 9 Finite element (FE) model for the stress intensity factor (SIF) calculation

tip (about 5×10^{-4} mm), progressively increasing to about 2 mm near the boundaries of the lower body. The applied SIFs in Mode I K_I and in Mode II K_{II} during the load pass were obtained from the displacements of the quarter nodes on the crack faces of the collapsed elements, according to the Williams equations:

$$
\begin{cases}
K_I = (v_2 - v_1) \dfrac{E \cdot \sqrt{\dfrac{2\pi}{r}}}{8(1-\nu^2)}, \\[4mm]
K_{II} = (u_2 - u_1) \dfrac{E \cdot \sqrt{\dfrac{2\pi}{r}}}{8(1-\nu^2)}
\end{cases}
\tag{22}
$$

where, as shown in Figure 9, v_1 and v_2 are the crack opening displacements (COD) of the quarter nodes of the elements at the crack tip, u_1 and u_2 are the crack shearing displacements (CSD) of the same nodes, $r = 1.25 \times 10^{-4}$ mm is the distance of the quarter nodes from the crack tip, and $E = 206{,}000$ MPa and $\nu = 0.3$ are the steel elastic modulus and coefficient of Poisson.

A fluid cavity interaction was imposed inside the crack, meaning that the volume of the crack cavity was kept constant during the whole simulation, as it was filled by an incompressible fluid. This is not exactly what happens when the load passes over the crack, because this model includes neither the fluid inlet when the crack mouth is opened nor the fluid squeezing when it is compressed near the tip region; however, it is able to reproduce the entrapped fluid pressurization when the crack mouth is closed, as shown in Figure 10.

Figure 11 shows the variation of K_I and K_{II} during a load pass in the case of the ER7 steel. K_I has a positive
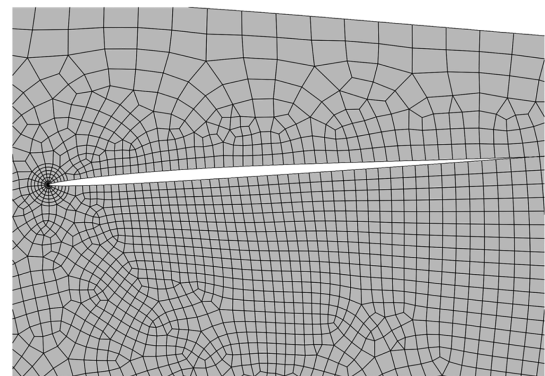

FIGURE 10 Finite element (FE) simulation of the entrapped fluid pressurization (the deformation is amplified six times)
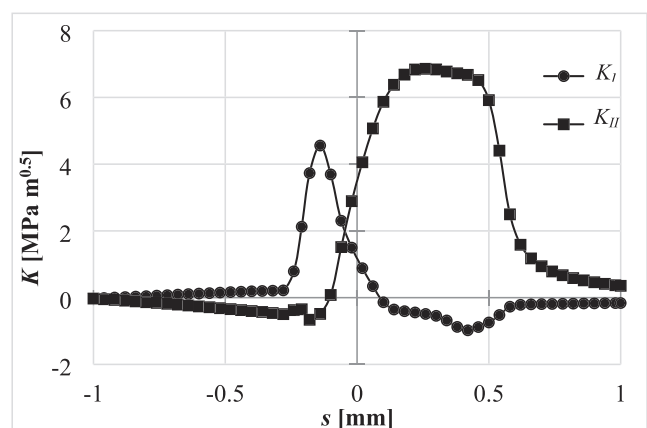

FIGURE 11 Variation of the stress intensity factors (SIFs) K_I and K_{II} during a load pass in the case of the ER7 typical crack

peak when the fluid is pressurized in the crack, then it has a slight negative peak. K_I should have only positive values if the crack was initially completely closed.

**TABLE 3** Results of the FAD assessment for the three tested steels

	ER7	Class B	Class B+
$\Delta\sigma_0$ (MPa)	841	983	1091
p_0 (MPa)	1219	1426	1581
ΔK_I (MPa m$^{0.5}$)	4.56	5.01	3.31
ΔK_{II} (MPa m$^{0.5}$)	7.52	6.69	6.35
ΔK_{eq} (MPa m$^{0.5}$)	9.29	8.99	7.48
p_p	0.90	0.77	0.70
k_p	1.15	1.27	1.00
p_{sh}/p_0	1.35	1.34	1.26
$\frac{K_Q(1-R)}{\Delta K_{thl.c.}}$	27.7	18.0	14.4

Abbreviation: FAD, Failure Assessment Diagram.

FIGURE 12 Failure Assessment Diagram (FAD) evaluation of the three tested steels in the wet contact step of the experimental tests. RCF, rolling contact fatigue [Colour figure can be viewed at wileyonlinelibrary.com]

However, the fluid cavity interaction requires a small initial crack opening, which explains small negative K_I values when the load completely closes the crack faces near the tip. This effect is slightly increased by the penalty method used for solving the contact, which allows a small interpenetration between the crack faces. The K_{II} variation is shifted toward the positive values, owing both to the presence of the friction on the contact surface and to the crack inclination. The SIF ranges were combined according to Equation (17) to obtain the mixed mode equivalent ΔK_{eq}.

Then, the k_p and p_p parameters could be calculated according to the previous equations (with $\Delta K = \Delta K_{eq}$), and the FAD was plotted for the three steels according to the material properties given in Table 1. Note that p_0 is calculated according to Equation (12) because the crack depth is much closer to the surface than to the depth where the maximum subsurface stress is located. The results are given in Table 3 and shown in Figure 12.

All the points representing the working conditions of the three tested steels exceed the fatigue limit and are placed in the region of high influence of the pre-existing cracks: This agrees with the damage observed at the end of the wet step of the tests. It is worth focusing on the case of the Class B+ specimen: Indeed, for this specimen, the p_p parameter is well lower than 1, whereas k_p is just equal to 1. This means that if a multiaxial fatigue criterion was used only, the specimen would be predicted in a safe condition; if a LEFM criterion was used only, the prediction would be uncertain, being the working point just on the border between the safe and unsafe condition. Using the FAD approach, instead, fatigue damage is clearly predicted, in full agreement with the experimental evidence.
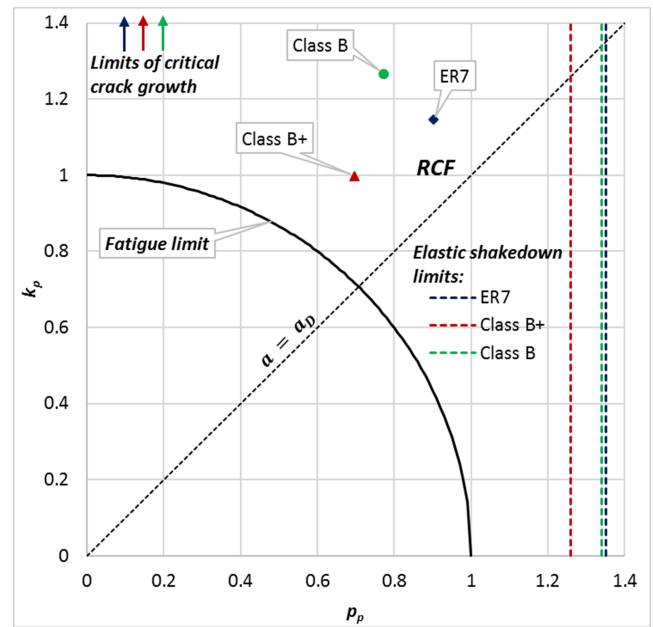
3.3 | Damage tolerant assessment

The FAD was used also to assess the problem according to a damage tolerant approach, for example, to determine the maximum tolerable defect size with respect to fatigue failure. For each steel, further finite element method (FEM) analyses were carried out decreasing the crack depth (with the same inclination as in the previous models), until the points representing the working condition in the FAD fell in the fatigue-safe region. By varying the crack size, the points of Figure 12 moved parallel to the ordinate, as only the k_p parameter was affected.

A failure index I can be introduced, defined as follows:

$$I = \sqrt{k_p^2 + p_p^2}. \tag{23}$$

Note that $I > 1$ when the working point is outside the fatigue-safe region; by decreasing the crack depth, I decreases as well until it intersects the fatigue limit curve for $I = 1$: the crack depth corresponding to this condition is the maximum allowable one.

Figure 13 shows the failure index I for the three steels with varying crack depth z. The condition $I = 1$ gives the following tolerable crack depths: $z \approx 15$ µm for the ER7 steel, $z \approx 19$ µm for the Class B+ steel, and $z \approx 21$ µm for the Class B steel. The lower allowable depth of the ER7
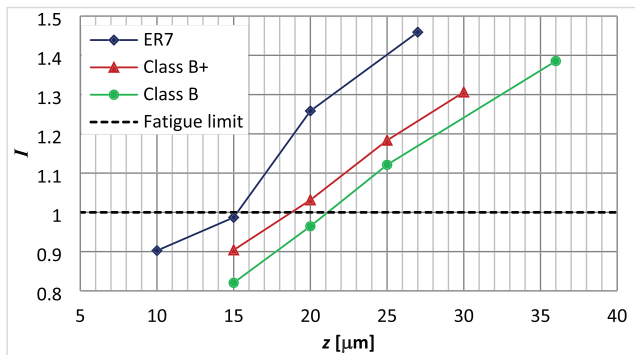
FIGURE 13 Determination of the maximum tolerable crack depth in the three tested steels [Colour figure can be viewed at wileyonlinelibrary.com]

steel is related to the p_p parameter: As it is closer to 1 with respect to the other steels, meaning that this steel works closer to the plain fatigue limit, a shallower crack is sufficient to start fatigue. Note that this happens despite the ER7 steel having a higher crack propagation threshold $\Delta K_{thl.\ c.}$ with respect to the other steels. Once again, this result shows that the combination of the LEFM and multiaxial fatigue criteria given by the FAD can lead to different conclusions with respect to following the single approaches.

These results are valid for the crack inclinations determined by the statistical analysis on the tested specimens. As the crack inclination affects the applied SIF, they cannot be extended as results of general validity. However, the SIF increases as far as the crack inclination decreases: As very low inclinations were detected for all the steels, these results can be taken as a lower bound for crack propagation.

4 | CONCLUSIONS

A FAD approach was proposed for the contact fatigue assessment of railway wheels. This approach allows combining multiaxial fatigue criteria with the LEFM approach, accounting for the influence of the size of pre-existing surface cracks. The specific dominant damage of railway wheels was assumed to be ratcheting in dry rolling-sliding contact, leading to the formation of surface cracks, followed by shelling in wet contact, driven by the pressurization of the previously formed cracks.

The FAD was used to assess the results of previous experimental tests on discs made with three railway wheel steels, subjected first to dry and subsequently to wet contact. The typical surface crack of each steel was statistically determined after the dry session. The FAD assessment allowed predicting RCF for all the steels, in agreement with the experimental results. In addition, the

FAD allowed determining the maximum acceptable crack depth for each steel.

This example of FAD application showed its potential as a damage tolerant approach for railway wheels. Indeed, it allows investigating more in depth a field of application not covered by the most widely used tools, such as the well-known shakedown maps; furthermore, by combining the LEFM approach with the multiaxial fatigue criteria, it allows consideration of the different influence that differently sized cracks can have on the fatigue limit, this way leading to a more complete assessment of damage in railway wheels.

CONFLICT OF INTEREST
The authors declare that there is no conflict of interest that could be perceived as prejudicing the impartiality of the research reported.

DATA AVAILABILITY STATEMENT
Data are available upon request from the authors.

AUTHOR CONTRIBUTIONS
Giorgio Donzella: Conceptualization; formal analysis. **Andrea Danesi**: Data curation; investigation. **Angelo Mazzù**: Formal analysis; methodology. **Candida Petrogalli**: Data curation; investigation. **Andrea Ghidini**: Resources; validation. **Michela Faccoli**: Data curation; investigation.

NOMENCLATURE
a	crack length
a_0	intrinsic crack length
a_D	critical crack length
b	Hertz contact half width
E	Young's modulus
f	coefficient of friction on the rolling surface
f_c	coefficient of friction between the crack faces
I	fatigue failure index
K_I	Mode I stress intensity factor
K_{II}	Mode I stress intensity factor
K_{IC}	fracture toughness
k_p	crack propagation parameter
K_p	crack propagation parameter at fatigue limit
K_Q	size-dependent fracture toughness
n_i	number of cracks detected in a single tested material
N	total number of cracks detected in all the tested materials

p	maximum applied Hertz pressure
p_0	limit Hertz pressure of rolling contact fatigue in a defect-free material
p_{cr}	critical Hertz pressure
p_n	probability density related to the number of cracks
p_p	plain fatigue parameter
P_p	plain fatigue parameter at fatigue limit
p_{sh}	limit Hertz pressure of elastic shakedown
p_z	probability density related to the crack depth
p_{zn}	probability density related to the crack depth and number
P_{zn}	cumulated probability related to the crack depth and number
r	distance from the crack tip
R	load ratio (ratio of the minimum to maximum load in a cycle)
R_1	wheel disc radius
R_2	rail disc radius
R_{eq}	equivalent radius
s	rolling distance
u_1, u_2	crack shearing displacements
v_1, v_2	crack opening displacements
x	crack extension along the rolling direction
y	shape factor
z	crack depth
α	rotation angle
ΔK	stress intensity factor range
ΔK_{I0}	Mode I stress intensity factor range (positive part)
ΔK_{II}	Mode II stress intensity factor range
ΔK_{eq}	equivalent stress intensity factor range
ΔK_{th}	threshold stress intensity factor range
$\Delta K_{thl.c.}$	long crack threshold stress intensity factor range
$\Delta \sigma_0$	reversed tensile fatigue limit for a defect-free material (double amplitude)
$\Delta \sigma_{cr}$	critical stress range
$\Delta \tau_0$	shear fatigue limit for a defect-free material (double amplitude)
ϑ	crack inclination
ν	coefficient of Poisson
σ_{uts}	ultimate tensile strength
σ_y	yield stress

ORCID

Giorgio Donzella https://orcid.org/0000-0002-6972-7035
Andrea Danesi https://orcid.org/0000-0002-3208-3643
Angelo Mazzù https://orcid.org/0000-0002-6074-3143
Candida Petrogalli https://orcid.org/0000-0002-1774-3914
Michela Faccoli https://orcid.org/0000-0001-7543-2172

REFERENCES

1. Pradhan S, Samantaray AK, Bhattacharyya R. Prediction of railway wheel wear and its influence on the vehicle dynamics in a specific operating sector of Indian railways network. *Wear*. 2018;406–407:92-104.

2. Lu Y, Yang Y, Wang J, Zhu B. Optimization and design of a railway wheel profile based on interval uncertainty to reduce circular wear. *Math Probl Eng*. 2020;9579510.

3. Handa K, Ikeuchi K, Morimoto F. Temperature-dependent wear of tread-braked railway wheels. *Wear*. 2020;452-453:203265.

4. Lewis R, Dwyer-Joyce RS, Olofsson U, et al. Mapping railway wheel material wear mechanisms and transitions. *P I Mech Eng F-J Rai*. 2010;224:125-137.

5. Faccoli M, Petrogalli C, Lancini M, Ghidini A, Mazzù A. Effect of desert sand on wear and rolling contact fatigue behaviour of various railway wheel steels. *Wear*. 2018;396–397:146-161.

6. Zhu Y, Wang WJ, Lewis R, Yan WY, Lewis SR, Ding HH. A review on wear between railway wheels and rails under environmental conditions. *J Tribol T ASME*. 2019;141(12):120801.

7. Lyu Y, Bergseth E, Olofsson U. Open system tribology and influence of weather condition. *Sci Rep UK*. 2018;6:32455.

8. Faccoli M, Provezza L, Petrogalli C, Ghidini A, Mazzù A. Effects of full-stops on shoe-braked railway wheel wear damage. *Wear*. 2019;428–429:64-75.

9. Faccoli M, Provezza L, Petrogalli C, Ghidini A, Mazzù A. A small-scale experimental study of the damage due to intermittent shoe braking on the tread of high-speed train wheels. *Tribol T*. 2020;63(6):1041-1050.

10. Franklin FJ, Kapoor A. Modelling wear and crack initiation in rails. *P I Mech Eng F-J Rai*. 2007;221:23-33.

11. Mazzù A, Petrogalli C, Faccoli M. An integrated model for competitive damage mechanisms assessment in railway wheel steels. *Wear*. 2015;322-323:181-191.

12. Esmaeili A, Walia MS, Handa K, et al. A methodology to predict thermomechanical cracking of railway wheel treads: from experiments to numerical predictions. *Int J Fatigue*. 2017;105:71-85.

13. Walia MS, Esmaeili A, Vernersson T, Lundén R. Thermomechanical capacity of wheel treads at stop braking: a parametric study. *Int J Fatigue*. 2018;113:407-415.

14. Mazzù A, Donzella G. A model for predicting plastic strain and surface cracks at steady-state wear and ratcheting regime. *Wear*. 2018;400:127-136.

15. Magel E, Kalousek J. Identifying and interpreting railway wheel defects. In: *Proc. International Heavy Haul Association Conference on Freight Car Trucks/Bogies, NRC Publication Archive*; 1996:5.7-5.20.

16. Deuce R, Ekberg A, Kabo E. Mechanical deterioration of wheels and rails under winter conditions—mechanisms and consequences. *P I Mech Eng F-J Rai*. 2019;233(6):640-648.

17. Mazzù A, Provezza L, Zani N, Petrogalli C, Ghidini A, Faccoli M. Effect of shoe braking on wear and fatigue damage of various railway wheel steels for high speed applications. *Wear*. 2019;434-435:203005.

18. Bodini I, Petrogalli C, Mazzù A, Pasinetti S, Kato T, Makino T. A vision-based approach for rolling contact fatigue evaluation in twin-disc tests on a railway wheel steel. *Tribol Mater Surf Interfaces*. 2020;1-10. https://doi.org/10.1080/17515831.2020.1825062

19. Sakalo V, Sakalo A, Rodikov A, Tomashevskiy S. Computer modeling of processes of wear and accumulation of rolling contact fatigue damage in railway wheels using combined criterion. *Wear*. 2019;432–433:102900.

20. Yang L, Hu M, Zhao D, Yang J, Zhou X. A method for assessing wheel fatigue reliability considering multiaxial stress state. *Adv Mech Eng*. 2020;12(1):1-14.

21. Sciammarella CA, Chen RJS, Gallo P, Berto F, Lamberti L. Experimental evaluation of rolling contact fatigue in railroad wheels. *Int J Fatigue*. 2016;91:158-170.

22. Makino T, Kato T, Hirakawa K. The effect of slip ratio on the rolling contact fatigue property of railway wheel steel. *Int J Fatigue*. 2012;36(1:68-79.

23. Zhao X, Wang Z, Wen Z, Wang H, Zeng D. The initiation of local rolling contact fatigue on railway wheels: an experimental study. *Int J Fatigue*. 2020;132:105354.

24. Dowling AR, Townley CHA. The effect of defects on structural failure: a two-criteria approach. *Int J Pres Ves pip*. 1975;3(2):77-107.

25. Yu H, Zou H, Li W, Zhai J, Liu L. Safety assessments of rails with crack defects based on SINTAP-FAD method. *China Mech Eng*. 2019;30(3):271-278.

26. Donzella G, Petrogalli C. A failure assessment diagram for components subjected to rolling contact loading. *Int J Fatigue*. 2010;32(2):256-268.

27. Donzella G, Mazzù A, Petrogalli C. Failure assessment of sub-surface rolling contact fatigue in surface hardened components. *Eng Fract Mech*. 2013;103:26-38.

28. Kitagawa H, Takahashi S. Applicability of fracture mechanics to very small cracks or the cracks in the early stage. In: *Proc. of 2nd International Conference on Mechanical Behaviour of Materials*. ASM; 1976:627-631.

29. El Haddad MH, Topper TH, Smith KN. Prediction of non-propagating cracks. *Eng Fract Mech*. 1979;11(3):573-584.

30. Yu MT, DuQuesnay DL, Topper TH. Notch fatigue behaviour of SAE1045 steel. *Int J Fatigue*. 1988;10(2):109-116.

31. Atzori B, Lazzarin P, Meneghetti G. Fracture mechanics and notch sensitivity. *Fatigue Fract Eng Mater Struct*. 2003;26(3):257-267.

32. Broszeit E, Zwirlein O. Internal stresses and their influence on material stresses in Hertzian contacts—calculations with different stress hypotheses. *J Tribol T ASME*. 1986;108(3):387-393.

33. Dang Van K, Maitournam MH. Rolling contact in railways: modeling, simulation and damage prediction. *Fatigue Fract Eng Mater Struct*. 2003;26(10):939-948.

34. Desimone H, Bernasconi A, Beretta S. On the application of Dang Van criterion to rolling contact fatigue. *Wear*. 2006;260 (4–5):567-572.

35. Ciavarella M, Monno F. A comparison of multiaxial fatigue criteria as applied to rolling contact fatigue. *Tribol Int*. 2010;43 (11):2139-2144.

36. Atzori B, Meneghetti G, Susmel L. Material fatigue properties for assessing mechanical components weakened by notches and defects. *Fatigue Fract Eng Mater Struct*. 2005;28(1–2):83-97.

37. Ren Z, Glodez S. Computational simulation of different parameters influencing the contact stress distribution. *Int J Eng Modelling*. 1998;11:49-57.

38. Johnson KL. Contact mechanics and the wear of metals. *Wear*. 1995;190(2):162-170.

39. Faccoli M, Ghidini A, Mazzù A. Changes in the microstructure and mechanical properties of railway wheel steels as a result of the thermal load caused by shoe braking. *Metall Mater Trans A*. 2019;50(4):1701-1714.

40. Faccoli M, Ghidini A, Mazzù A. Experimental and numerical investigation of the thermal effects on railway wheels for shoe-braked high-speed train applications. *Metall Mater Trans a*. 2018;49(10):4544-4554.